Magnetic order in a Fermi gas induced by cavity-field fluctuations

Jingtao Fan,[1,2] Xiaofan Zhou,[1,2] Wei Zheng,[3,*] Wei Yi,[4,5,†] Gang Chen,[1,2,‡] and Suotang Jia[1,2]

[1]*State Key Laboratory of Quantum Optics and Quantum Optics Devices, Institute of Laser Spectroscopy, Shanxi University, Taiyuan 030006, China*

[2]*Collaborative Innovation Center of Extreme Optics, Shanxi University, Taiyuan, Shanxi 030006, China*

[3]*T.C.M. Group, Cavendish Laboratory, J. J. Thomson Avenue, Cambridge CB3 0HE, United Kingdom*

[4]*Key Laboratory of Quantum Information, University of Science and Technology of China, CAS, Hefei, Anhui 230026, China*

[5]*Synergetic Innovation Center of Quantum Information and Quantum Physics, University of Science and Technology of China, Hefei, Anhui 230026, China*

(Received 30 January 2018; published 12 October 2018)

We show that cavity-field fluctuations can induce interesting magnetic phases and phase transitions in an atom-cavity coupled system. Adopting a numerical density-matrix-renormalization-group method, we study the steady state of a two-component Fermi gas subject to cavity-assisted Raman coupling in a one-dimensional lattice at half filling. The cavity-enhanced atom-photon coupling introduces a dynamic long-range interaction in the atoms, which competes with the short-range on-site interactions and leads to a rich phase diagram with a variety of magnetic orders. Importantly, as all the phase transitions take place outside the superradiant regime, the magnetic orders are associated with cavity-field fluctuations with a vanishing number of photons on the mean-field level.

DOI: 10.1103/PhysRevA.98.043613

I. INTRODUCTION

Coherently driven atomic gases inside optical cavities have attracted much research interest of late [1]. In these systems, as the atoms serve as a nonlinear media between the external pumping and the cavity field, cavity photons feed back on the atomic degrees of freedom, effectively imposing a dynamic potential on atoms. These dynamic potentials are responsible for interesting nonequilibrium collective dynamics and exotic steady states, which are the subjects of intensive experimental and theoretical study [2–38] .

Recently, a series of seminal experiments has demonstrated the impact of various dynamic potentials on atomic gases inside cavities [2–8]. A prominent example is the observation of the supersolid phase transition in a transversely pumped Bose-Einstein condensate coupled to a cavity [2–4]. In the experiment, as the cavity field becomes superradiant, the back action of the photons induces a dynamic superlattice potential and drives atoms into a self-organized steady state. Further, it has been predicted theoretically [9–14] and subsequently experimentally verified [5–8] that cavity-induced dynamic long-range interactions can lead to a rich phase diagram for a Bose-Hubbard model inside a cavity. Meanwhile, much theoretical effort has been dedicated to the study of cavity-assisted dynamic gauge potentials, both Abelian [15–19] and non-Abelian [20–26], in atom-photon ensembles, with the prospect of generating anomalous nonequilibrium dynamics [15–17] or steady states with exotic phases and correlations [18–24]. Whereas most previous studies focus on the superradiant regime, where the cavity field is essentially in a coherent state, the cavity-field fluctuations become crucial away from superradiance. An intriguing question is then the clarification of the impact of cavity-field fluctuations on atoms.

In this work, we show that fermions coupled to a cavity can develop interesting magnetic phases under the dynamic long-range interaction driven by cavity-field fluctuations. We focus on the steady state of a two-component Fermi gas in a one-dimensional optical lattice coupled to a cavity via the Raman transition. The fermions can be effectively described by an extended Hubbard model with both on-site and dynamic long-range interactions [27]. As the long-range interaction features spin-flipping processes, it competes with the spin-conserving on-site interactions and leads to the emergence of magnetic correlations and, consequently, various magnetic orders in the steady state.

Adopting the numerical density-matrix-renormalization-group (DMRG) method, we map out the steady-state phase diagram and demonstrate that, as the cavity parameters are tuned, the system is driven from an antiferromagnetic state to a ferromagnetic state, with various anisotropic magnetic orders lying in-between. As magnetic phase transitions take place in an effectively blue-detuned cavity in the absence of superradiance, they are driven by cavity-field fluctuations rather than the superradiance. Our work is therefore in sharp contrast to previous theoretical and experimental studies [2–12,15–38], where the focus has been on the phenomena induced by the superradiance.

The work is organized as follows. In Sec. II, we describe the proposed system configuration and present the effective Hamiltonian. In Sec. III, we calculate the phase diagram

*zhengwei8796@gmail.com
†wyiz@ustc.edu.cn
‡chengang971@163.com

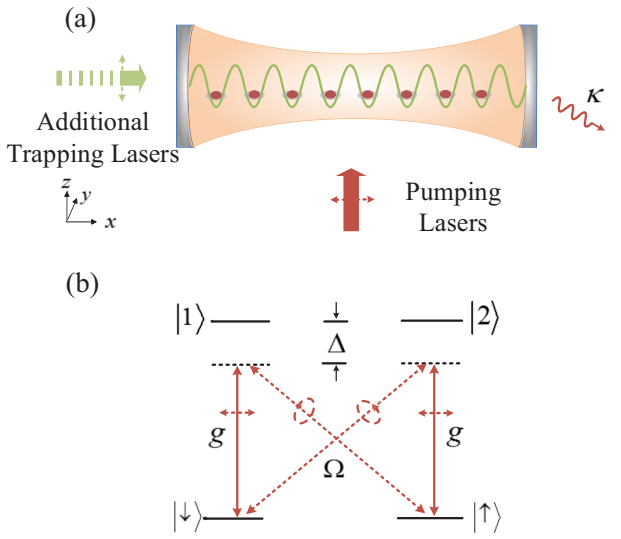

FIG. 1. (a) Fermions in a one-dimensional lattice potential are loaded into a high-finesse optical cavity, which is subject to a linearly polarized transverse pumping laser. (b) The pumping laser and the cavity field couple two hyperfine states in two separate Raman processes. See the main text for the definitions of the labels.

and characterize the effects of cavity-induced long-range interactions using the DMRG approach. We discuss in detail the fluctuation-induced magnetic phases in Sec. IV, and we summarize in Sec. V.

II. MODEL

We consider a two-component Fermi gas in a quasi-one-dimensional optical lattice potential inside a high-finesse optical cavity. As shown in Fig. 1, while the lattice and the cavity are aligned along the x axis, the atoms are tightly confined in the transverse directions so that only the atomic motion along the x direction is relevant. The cavity is subject to a transverse pumping laser, which, together with the cavity field, couples the two hyperfine states ($\{|\downarrow\rangle, |\uparrow\rangle\}$) of the fermions in two separate Raman processes (we take the z direction as the quantization axis). The cavity frequency ω_c is close to that of the pumping laser ω_p, both of which are red-detuned from the electronically excited states ($\{|1\rangle, |2\rangle\}$) with large single-photon detuning $\Delta \gg g$ and Ω. Here g is the single-photon Rabi frequency of the cavity field, and Ω is the Rabi frequency of the pumping laser.

By adiabatically eliminating the excited states and adopting the tight-binding approximation, the Hamiltonian of the system can be written as (see Appendix A for details, $\hbar = 1$ throughout)

$$\hat{H} = \left(\Delta_c - M_1 \sum_{j,\sigma} \hat{n}_{j\sigma}\right)\hat{a}^\dagger \hat{a} - t\sum_{j,\sigma}(\hat{c}^\dagger_{j\sigma}\hat{c}_{j+1\sigma} + \text{H.c.}) + \eta\left(\hat{a}^\dagger + \hat{a}\right)M_0 \sum_j (-1)^j (\hat{c}^\dagger_{j\uparrow}\hat{c}_{j\downarrow} + \hat{c}^\dagger_{j\downarrow}\hat{c}_{j\uparrow}) + \frac{U_s}{2}\sum_j \hat{n}_{j\uparrow}\hat{n}_{j\downarrow}, \quad (1)$$

where $(\hat{a}, \hat{a}^\dagger)$ are the field operators for the cavity photons in the frame rotating with the frequency ω_p, $c^\dagger_{j\sigma}$ $(c_{j\sigma})$ creates (annihilates) a fermion with spin σ $(\sigma = \uparrow, \downarrow)$ on site j, and the density operator $\hat{n}_{j\sigma} = \hat{c}^\dagger_{j\sigma}\hat{c}_{j\sigma}$. The cavity detuning is given by $\Delta_c = \omega_c - \omega_p$, and the effective pumping strength $\eta = \nu g\Omega/\Delta$, with the constant ν coming from transverse integrals [22]. U_s and t are respectively the on-site interaction strength and the lattice hopping rate. We also have $M_1 = \frac{g^2}{\Delta}\int dx W_j^* \cos^2(k_0 x) W_j$ and $M_0 = \int dx W_0^* \cos(k_0 x) W_0$, where W_j is the Wannier function centered at site j and k_0 is the wave vector of the cavity field. Here we have assumed that the background lattice potential is much deeper than cavity-field shifts, such that the Wannier functions as well as U_s and t are approximately static. We have also neglected the Zeeman terms of the hyperfine spins, which corresponds to a vanishing external magnetic field. We have checked that our main results are robust under a small Zeeman field (see Appendix B).

Taking the cavity decay into account, we derive the steady-state solution $\partial_t \hat{a} = 0$ from the Heisenberg equations

$$\hat{a} = \frac{\eta M_0}{i\kappa + \tilde{\delta}} \sum_j (-1)^j (\hat{c}^\dagger_{j\uparrow}\hat{c}_{j\downarrow} + \hat{c}^\dagger_{j\downarrow}\hat{c}_{j\uparrow}), \quad (2)$$

where κ is the cavity decay rate, the effective cavity detuning $\tilde{\delta} = NM_1 - \Delta_c$, and N is the total atom number. The factor $(-1)^j$, also appearing in Hamiltonian (A7), derives from the spatial dependence of the Raman potential associated with M_0, which has twice the period of the background lattice potential. The Raman potential and hence the on-site spin-flipping terms have opposite signs on adjacent sites (see Appendix A).

Importantly, the steady-state cavity field $\hat{a}$ is associated with the antiferromagnetic spin correlations along the x direction, as $\hat{a} \propto \sum_j (-1)^j \hat{C}^\dagger_j \sigma_x \hat{C}_j$, where σ_x is the corresponding Pauli matrix and $C_j = (c_{j\uparrow}, c_{j\downarrow})^T$. Whereas such a relation plays a key role in driving fermions into the magnetically ordered phases, this point becomes immediately clear if we adiabatically eliminate the cavity field in the large-decay limit [27], where the energy of the atomic motion is much smaller than that of photons. The resulting effective Hamiltonian of fermions is essentially an extended Hubbard model with both on-site and dynamic long-range interactions:

$$\hat{H} = -t\sum_{j,\sigma}(\hat{c}^\dagger_{j\sigma}\hat{c}_{j+1\sigma} + \text{H.c.}) + \frac{U_s}{2}\sum_j \hat{n}_{j\uparrow}\hat{n}_{j\downarrow} + \frac{U_l}{L}\left[\sum_j (-1)^j (\hat{c}^\dagger_{j\uparrow}\hat{c}_{j\downarrow} + \hat{c}^\dagger_{j\downarrow}\hat{c}_{j\uparrow})\right]^2. \quad (3)$$

Here $U_l/L = |\eta M_0|^2 \tilde{\delta}/(\tilde{\delta}^2 + \kappa^2)$, where L is the total number of lattice sites. Note that while t and U_s can be tuned by adjusting lattice parameters, the long-range interaction strength U_l can be tuned over a wide range by adjusting parameters such as Ω, $\tilde{\delta}$, and g. Note that we are working in the regime with $\kappa \gg \eta$, where dissipative processes play a minor role [33].

The competition of the spin-preserving on-site interactions (characterized by U_s) and the spin-flipping long-range

interactions (characterized by U_l) can give rise to interesting magnetically ordered phases. This is particularly true if we consider a repulsive on-site interaction with $U_s > 0$, where it is well known that an isotropic antiferromagnetic order is favored at half filling when $U_l = 0$ [39–43]. In contrast, for large and positive U_l, the formation of an antiferromagnetic order along the x direction would be hindered, and the system should favor a ferromagnetic order along the x direction. Therefore, a quantum phase transition should occur between these limiting cases. Further, as the dynamic long-range interaction breaks the SO(3) symmetry of the original Hubbard model into an SO(2) rotational symmetry around the x axis, the magnetic orders should in general be anisotropic.

To clarify the impact of the dynamic long-range interaction on the magnetism of the steady state, in the following, we perform numerical simulations using the DMRG calculations, for which we retain 150 truncated states per DMRG block and perform 20 sweeps with a maximum truncation error $\sim 10^{-5}$. We focus on a half-filled lattice ($N/L = 1$) with repulsive on-site interactions $U_s > 0$ under open boundary conditions.

III. EFFECT OF THE DYNAMIC LONG-RANGE INTERACTION

The existence of the magnetic order can be characterized by the static spin structure factor [44–47]

$$S_\alpha(k) = \frac{1}{L}\sum_{l,j} e^{ik(l-j)}\langle \hat{s}_l^\alpha \hat{s}_j^\alpha \rangle, \tag{4}$$

where $\hat{s}_j^\alpha = \frac{1}{2}C_j^\dagger \sigma_\alpha C_j$ and σ_α ($\alpha = x, y, z$) are the Pauli matrices. As the position of peaks in $S_\alpha(k)$ characterizes the spatial variation of spin orientations projected into the α direction, peaks at $k = \pm\pi$ and $k = 0$ represent respectively antiferromagnetic and ferromagnetic orders in the corresponding direction [44–47]. Alternatively, we can characterize the magnetic order using the spin correlation function

$$C_\alpha(r) = \frac{1}{L}\sum_{l} \langle \hat{s}_l^\alpha \hat{s}_{l+r}^\alpha \rangle, \tag{5}$$

where r is the distance between different sites. The advantage of $C_\alpha(r)$ is that it offers an intuitive picture of the spatial distribution of the spin correlations [46–54]. More specifically, for an antiferromagnetic state, the sign of $C_\alpha(r)$ should alternate as r increases; while for phases with dominantly ferromagnetic correlations, $C_\alpha(r)$ should become purely positive [47–53].

We first study the variation of $S_\alpha(k)$ ($\alpha = x, z$) with different values of U_l at a fixed $t/U_s = 0.1$. As illustrated in Figs. 2(a) and 2(b), when $U_l = 0$, $S_z(k)$ and $S_x(k)$ peak identically at $k = \pm\pi$, which is consistent with the existence of an isotropic antiferromagnetic order in the ground state of a repulsive Hubbard model at half filling. This is further confirmed by the spin correlations, as $C_z(r)$ and $C_x(r)$ oscillate identically around zero as r increases [see Figs. 2(c) and 2(d)]. For finite U_l however, the system is only isotropic in the transverse directions, which is reflected in the drastically different peak structures along the x direction and the z direction when $U_l \neq 0$.

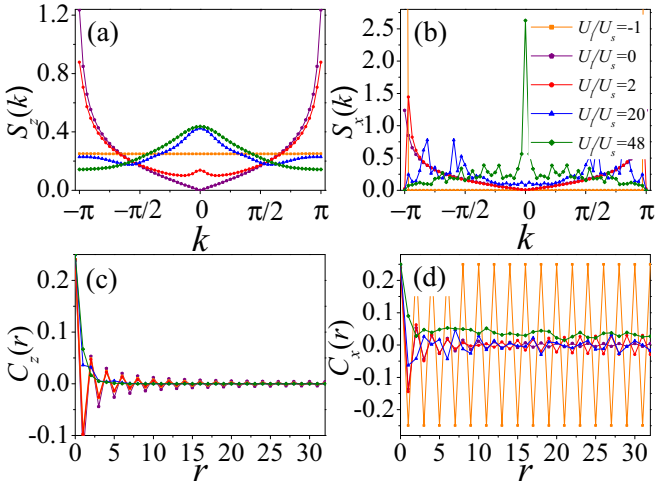

FIG. 2. Spin structure factors (a) $S_z(k)$ and (b) $S_x(k)$ and spin correlation functions (c) $C_z(r)$ and (d) $C_x(r)$ for systems with $t/U_s = 0.1$, $L = 64$, and a varying U_l/U_s.

For $U_l < 0$, the system features anisotropic antiferromagnetic orders along the x direction and the z direction, as $S_z(k)$ and $S_x(k)$ still peak at $k = \pi$ but with different peak structures. The spin correlations also behave differently along the two directions. Whereas the oscillations in $C_z(r)$ exhibit a power-law decay, $C_x(r)$ appears to be undamped, suggesting long-range antiferromagnetic order. Note that, as the dynamic interaction is of infinitely long range, the emergence of long-range correlations in one dimension is understandable.

As U_l becomes positive, a new peak at $k = 0$ immediately emerges in $S_z(k)$, which suggests the building up of ferromagnetic correlations. The peak at $k = 0$ eventually becomes higher than that at $k = \pi$, as U_l is increased beyond a critical value of $U_l/U_s \approx 16$, which we associate with a transition from antiferromagnetism to ferromagnetism in the transverse direction. Such a transition can be confirmed by the spin correlations, as $C_z(r)$ becomes purely positive beyond the critical U_l.

The situation along the x direction is more complicated. As soon as U_l becomes positive, the peak in $S_x(k)$ is shifted away from $k = \pi$. This suggests that the spin orientations become noncollinear in the x direction, which we identify as an incommensurate antiferromagnetic order [55]. In the incommensurate antiferromagnetic state, $C_x(r)$ still features oscillations around zero, but with periods incommensurate with that of the lattice. At larger U_l, the competition between the on-site and the long-range interactions gives rise to multiple peaks in $S_x(k)$, which eventually merge into a single one at $k = 0$ when U_l is increased above a critical value of $U_l/U_s \approx 27$. Therefore, when the long-range interaction is strong enough, the system becomes ferromagnetic along both the x direction and the transverse directions, where both $C_z(r)$ and $C_x(r)$ become purely positive.

With the understanding above, we map out the phase diagram of the system in the U_l-t plane. The magnetic orders are identified from the peak locations in the corresponding structure factors (see Table I for detailed descriptions). For example, the phase boundaries for the ferromagnetic orders

TABLE I. The correspondence between ϑ_α and different magnetic phases, where ϑ_α denotes the position of the highest peak in $S_\alpha(k)$ ($\alpha = x$ and z).

Position of peak	AF	FM	AF_z-IAF_x	FM_z-IAF_x
ϑ_z	$\pm\pi$	0	$\pm\pi$	0
ϑ_x	$\pm\pi$	0	$\neq 0, \pm\pi$	$\neq 0, \pm\pi$

are determined by requiring the peak at $k = 0$ be equal in height to the highest peak elsewhere. Phase boundaries determined from peaks in the spin structure factors are consistent with those calculated from the signs of the spin correlation functions (see Appendix C).

As shown in Fig. 3, in the transverse directions, the system changes from an antiferromagnetic phase to a ferromagnetic phase at positive U_l. While in the x direction, the steady state is antiferromagnetic for $U_l < 0$, incommensurate antiferromagnetic for intermediate U_l, and ferromagnetic in the large U_l limit. The magnetic order is indeed anisotropic in general. Note that as the phase diagram is obtained for a finite-size lattice, we have numerically confirmed its validity in the thermodynamic limit $L \to \infty$ using a finite-size-scaling analysis (see Appendix D).

IV. CAVITY-FIELD FLUCTUATIONS

As the cavity field is associated with the antiferromagnetic correlations according to Eq. (2), it serves as the driving force behind magnetic transitions. To further clarify the role and the behavior of cavity photons throughout the phase transitions, in Fig. 4, we plot the number of cavity photons $\langle\hat{a}^\dagger\hat{a}\rangle$ in the steady state with varying U_l. For comparison, we also show the square of the mean cavity field $|\langle\hat{a}\rangle|^2$, which should be close to $\langle\hat{a}^\dagger\hat{a}\rangle$ when the mean-field approximation $\hat{a} \approx \langle\hat{a}\rangle$ is valid.

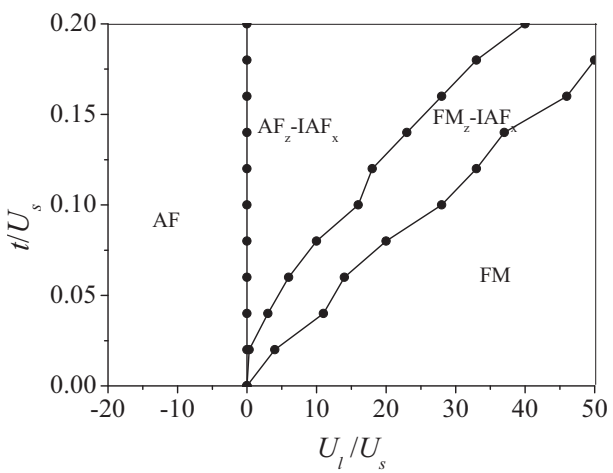

FIG. 3. The phase diagram in the U_l-t plane for a system with $L = 64$. AF, FM, and IAF correspond to antiferromagnetic state, ferromagnetic state, and incommensurate antiferromagnetic state, respectively, with the subscripts indicating the direction of the magnetic order. The definitions of the different phases are listed in Table I.

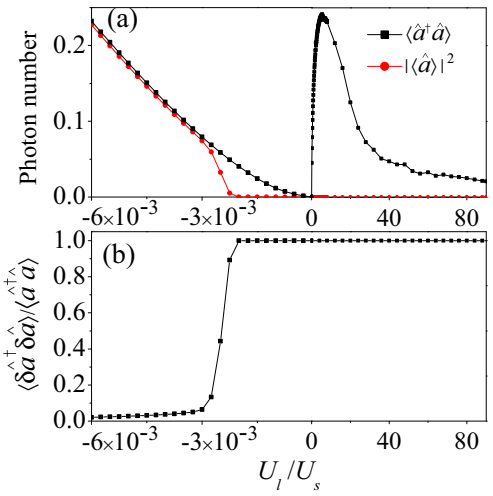

FIG. 4. (a) The cavity photon number and (b) the cavity-field fluctuation $\langle\delta\hat{a}^\dagger\delta\hat{a}\rangle/\langle\hat{a}^\dagger\hat{a}\rangle$ as a function of U_l, where we have taken $t/U_s = 0.1$, $\tilde{\delta}/U_s = 1$, and $L = 64$.

In Fig. 4(a), at a first glance, we can identify a superradiant transition, where $|\langle\hat{a}\rangle|^2$ becomes finite, for an effectively red-detuned cavity ($\tilde{\delta} < 0$, $U_l < 0$). As U_l decreases further, $|\langle\hat{a}\rangle|^2$ increases and rapidly approaches $\langle\hat{a}^\dagger\hat{a}\rangle$. This indicates that the cavity field can be described by a coherent state when the system is in the superradiant regime.

In contrast, in the region where the cavity is effectively blue-detuned ($\tilde{\delta} > 0$, $U_l > 0$) and where all the magnetic phase transitions take place, the cavity is not superradiant, as $|\langle\hat{a}\rangle|^2$ remains vanishingly small. This is consistent with a recent experiment [38], where the absence of superradiance has been reported for a blue-detuned cavity. In this region, the cavity is dominated by fluctuations as $|\langle\hat{a}\rangle|^2$ deviates considerably from the photon number $\langle\hat{a}^\dagger\hat{a}\rangle$. In Fig. 4(b), we characterize cavity-field fluctuations with $\langle\delta\hat{a}^\dagger\delta\hat{a}\rangle/\langle\hat{a}^\dagger\hat{a}\rangle$ ($\delta\hat{a} = \hat{a} - \langle\hat{a}\rangle$), which vanishes in a coherent state and approaches unity in the case of large cavity fluctuations. Apparently, both the incommensurate antiferromagnetic and the ferromagnetic orders are induced by the cavity-field fluctuations instead of superradiance.

With increasing U_l, the cavity photon number undergoes a nonmonotonic change, with a peak situated at $U_l/U_s \approx 5.5$. To understand this behavior, we can relate the cavity photon number to the structure factor:

$$\langle\hat{a}^\dagger\hat{a}\rangle = 4\frac{U_l}{\tilde{\delta}}S_x(k = \pi). \tag{6}$$

According to Eq. (6), the steady-state photon number is collectively determined by both U_l and the static structure factor $S_x(k = \pi)$. Therefore, an antiparallel spin configuration will feed back positively on the cavity photon number and vice versa. In the absence of the atom-photon coupling ($U_l = 0$), the photon number is equal to zero, and the fermions are in the antiferromagnetic state. A small and positive U_l is not sufficient to break the intrinsic antiferromagnetic order of the system, which in turn gives rise to an increase of the photon number. By increasing U_l further, the ferromagnetic configuration starts to dominate, which will then decrease

the photon number. In the large-U_l limit, the average photon number monotonically approaches zero, as the steady state acquires an anisotropic ferromagnetic order. While the lack of superradiance for $U_l > 0$ is consistent with mean-field results with $U_s = 0$ (see Appendix E), the characterization of the steady-state in this region is clearly beyond the mean-field approach.

Finally, as the long-range cavity-induced interaction U_l drives ferromagnetic phase transitions, transition temperatures can be estimated using the values of U_l on the corresponding phase boundaries in Fig. 3. Importantly, the value of U_l can be quite large under typical experimental parameters. For example, adopting typical parameters of ^{6}Li atoms and fixing the transverse harmonic confinement frequency, the recoil energy, and the hopping rate as $\omega_{y,z} = 2\pi \times 22.5$ kHz, $E_r = 73.7$ kHz, and $t/U_s = 0.1$, respectively, the estimated transition temperature for FM_z-IAF_x is $\sim 6\,\mu$K, while that for FM is $\sim 10\,\mu$K. These temperatures are quite accessible under current experimental conditions for fermions in optical lattice potentials [45,52,56].

V. CONCLUSION

We have shown that magnetic phases and phase transitions can be induced by cavity-field fluctuations away from the superradiant regime. Such a behavior is drastically different from previous studies focusing on the effects of superradiance, where the mean-field approach is applicable. Magnetic phase transitions lead to signals in the spin dynamic structure factor, which can be detected by measuring the photons leaking out of the cavity [57]. Alternatively, magnetic orders can be probed by constructing the spin correlation function from spin-resolved *in situ* measurements [51,56]. In a very recent experiment [58], spin textures have been probed in the steady state of a quantum gas inside the cavity, which indicates that experimental tools for probing magnetism in atom-cavity hybrid systems are already available.

ACKNOWLEDGMENTS

We thank Yu Chen for helpful discussions. This work is supported partly by the National Key R&D Program of China under Grants No. 2017YFA0304203 and No. 2016YFA0301700; the NKBRP under Grant No. 2013CB922000; the NSFC under Grants No. 60921091, No. 11434007, No. 11522545, No. 11674200, and No. 11804204; the PCSIRT under Grant No. IRT13076; SFSSSP; OYTPSP; and 1331KYC. W.Z. acknowledges support from EPSRC Grant No. EP/K030094/1.

J.F. and X.Z. contributed equally to this work.

APPENDIX A: EFFECTIVE HAMILTONIAN

In this section, we provide more details on the derivation of Hamiltonian (1) in the main text. We start by considering the coupling of internal states of a single atom, as illustrated in Fig. 1(b) in the main text. The Hamiltonian can be written as $\hat{H}^{(1)} = \hat{H}_0^{(1)} + \hat{H}_{\rm I}^{(1)}$, where

$$\hat{H}_0^{(1)} = \sum_{i=1,2,\uparrow,\downarrow} \omega_i |i\rangle\langle i| + \omega_c \hat{a}^\dagger \hat{a}, \tag{A1}$$

$$\hat{H}_{\rm I}^{(1)} = -\Omega(|1\rangle\langle\uparrow| + |2\rangle\langle\downarrow|)e^{-i(\omega_p t + k_0 z)} - g(x)[|1\rangle\langle\downarrow|\hat{a} + |2\rangle\langle\uparrow|\hat{a}] + \text{H.c.} \tag{A2}$$

In the Hamiltonians (A1) and (A2), ω_i denotes the eigenfrequency of the atomic state $|i\rangle$ ($i = 1, 2, \uparrow$, and $\downarrow$). The field operator $\hat{a}$ describes the annihilation of a cavity photon with the frequency ω_c. The Raman channels are driven by the two circularly polarized components of the transverse pumping laser with the frequency ω_p and the single-photon Rabi frequency Ω. The space-dependent atom-cavity coupling is given by $g(x) = g\cos(k_0 x)$ ($j = 1$ and 2), where g_j is the coupling constant and k_0 is the cavity-field wave vector. H.c. denotes the Hermitian conjugation.

We introduce a time-dependent unitary transformation, $\hat{U}(t) = \exp[i(\sum_{\sigma=\uparrow,\downarrow} |\sigma\rangle\langle\sigma| + a^\dagger a)\omega_p t]$, under which $\hat{H}^{(1)}$ becomes

$$\hat{H}^{(1)} = \Delta_c \hat{a}^\dagger \hat{a} + \Delta|1\rangle\langle 1| + \Delta|2\rangle\langle 2| - [g\cos(k_0 x)|1\rangle\langle\downarrow|\hat{a} + g\cos(k_0 x)|2\rangle\langle\uparrow|\hat{a} + \Omega|1\rangle\langle\uparrow| + \Omega|2\rangle\langle\downarrow| + \text{H.c.}] + m_z(|\uparrow\rangle\langle\uparrow| - |\downarrow\rangle\langle\downarrow|), \tag{A3}$$

where $\Delta_c = \omega_c - \omega_p$ is the cavity detuning, $\Delta = \omega_1 - \omega_p \approx \omega_2 - \omega_p$ denotes the single-photon detuning, and $m_z = (\omega_\uparrow - \omega_\downarrow)/2$ is the Zeeman energy. We work in the limit of large single-photon detuning $|\Delta| \gg \{|\Omega|, |g|, |\Delta_c|\}$, which allows us to adiabatically eliminate the excited states $|1\rangle$ and $|2\rangle$. The resulting effective Hamiltonian is given as

$$\hat{H}^{(1)} = \omega \hat{a}^\dagger \hat{a} + \eta_0 \cos(k_0 x)(|\downarrow\rangle\langle\uparrow| + |\uparrow\rangle\langle\downarrow|)(\hat{a}^\dagger + \hat{a}) + m_z(|\uparrow\rangle\langle\uparrow| - |\downarrow\rangle\langle\downarrow|), \tag{A4}$$

where $\omega = \Delta_c - \varepsilon\cos^2(k_0 x)$ and $\eta_0 = g\Omega/\Delta$, with $\varepsilon = |g|^2/\Delta$.

To describe the dynamics of N atoms in a background lattice potential and with inter-atomic interactions, we extend the single-particle Hamiltonian $\hat{H}^{(1)}$ to the second-quantized form

$$\hat{H} = \Delta_c \hat{a}^\dagger \hat{a} + \sum_\sigma \int d^3\mathbf{r}\hat{\Psi}_\sigma^\dagger(\mathbf{r})\left[\frac{\hat{\mathbf{p}}^2}{2m} + (V_0 - \varepsilon\hat{a}^\dagger\hat{a})\times\cos^2(k_0 x) + V_R(\mathbf{r})\right]\hat{\Psi}_\sigma(\mathbf{r}) + \eta_0\cos(k_0 x)(\hat{a}^\dagger + \hat{a}) \times \int d^3\mathbf{r}[\hat{\Psi}_\uparrow^\dagger(\mathbf{r})\hat{\Psi}_\downarrow(\mathbf{r}) + \hat{\Psi}_\downarrow^\dagger(\mathbf{r})\hat{\Psi}_\uparrow(\mathbf{r})] + \frac{U_0}{2}\int d^3\mathbf{r}\hat{\Psi}_\uparrow^\dagger(\mathbf{r})\hat{\Psi}_\downarrow^\dagger(\mathbf{r})\hat{\Psi}_\downarrow(\mathbf{r})\hat{\Psi}_\uparrow(\mathbf{r}) + m_z\int d^3\mathbf{r}[\hat{\Psi}_\uparrow^\dagger(\mathbf{r})\hat{\Psi}_\uparrow(\mathbf{r}) - \hat{\Psi}_\downarrow^\dagger(\mathbf{r})\hat{\Psi}_\downarrow(\mathbf{r})], \tag{A5}$$

where $\hat{\Psi}_\sigma(\mathbf{r})$ denotes the field operator for annihilating an atom with spin σ ($\sigma = \uparrow$ and $\downarrow$) at position $\mathbf{r}$, and $U_0 \equiv 4\pi a_s \hbar^2/m$ models a two-body short-range interaction, with a_s being the s-wave scattering length. In Eq. (A5), besides the kinetic-energy term $\hat{\mathbf{p}}^2/2m$, the background optical lattice $V_0\cos^2(k_0 x)$ ($V_0 < 0$) and the transverse trapping

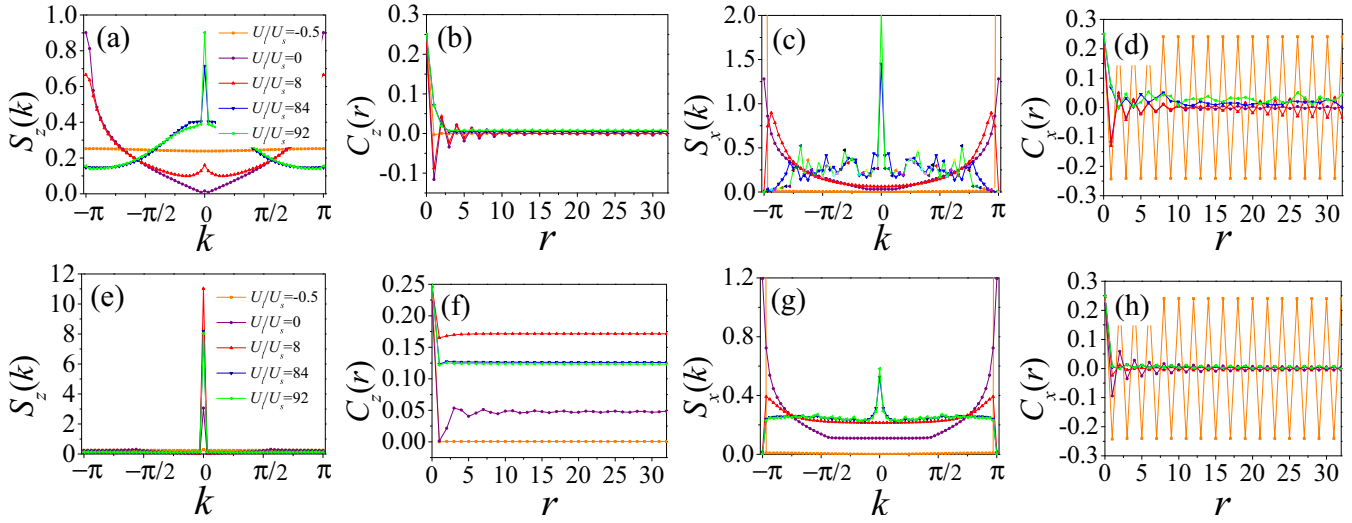

FIG. 5. Spin structure factors and spin correlation functions for systems with $t/U_s = 0.2$, $L = 64$, and a varying U_l. The top panels [panels (a)–(d)] correspond to $m_z/U_s = 0.01$ and the bottom panels [panels (e)–(h)] correspond to $m_z/U_s = 0.05$.

potential $V_R(\mathbf{r})$ are added. We further assume $V_R(\mathbf{r})$ is strong enough so that the atomic motion in the transverse direction is frozen to the ground state. This enables us to integrate out the transverse degrees of freedom using $\hat{\Psi}_\sigma(\mathbf{r}) = \sqrt{2/\pi\rho^2}\hat{\psi}_\sigma(x)\exp[-(y^2+z^2)/\rho^2]$, where ρ is a transverse characteristic length. The simplified one-dimensional Hamiltonian thus reads

$$\begin{aligned}\hat{H} = {} & \Delta_c\hat{a}^\dagger\hat{a} + \sum_\sigma \int dx\,\hat{\psi}^\dagger_\sigma(x)\left[\frac{\hat{p}_x^2}{2m} + (V_0 - \varepsilon\hat{a}^\dagger\hat{a})\cos^2(k_0x)\right] \\ & \times \hat{\psi}_\sigma(x) + \frac{U}{2}\int dx\,\hat{\psi}^\dagger_\uparrow(x)\hat{\psi}^\dagger_\downarrow(x)\hat{\psi}_\downarrow(x)\hat{\psi}_\uparrow(x) \\ & + \eta\cos(k_0x)\left(\hat{a}^\dagger + \hat{a}\right)\int dx[\hat{\psi}^\dagger_\uparrow(x)\hat{\psi}_\downarrow(x) + \hat{\psi}^\dagger_\downarrow(x)\hat{\psi}_\uparrow(x)] \\ & + m_z\int dx[\hat{\psi}^\dagger_\uparrow(x)\hat{\psi}_\uparrow(x) - \hat{\psi}^\dagger_\downarrow(x)\hat{\psi}_\downarrow(x)], \end{aligned} \tag{A6}$$

where $U = U_0/(\pi\rho^2)$ and $\eta = \nu\eta_0$, with $\nu = \exp(-k_0^2\rho^2/8)$.

Assuming a deep background lattice potential with $|V_0| \gg \varepsilon\langle\hat{a}^\dagger\hat{a}\rangle$, we expand the field operator $\hat{\psi}_\sigma(x)$ in terms of the lowest-band Wannier functions $W(x - x_j)$ of the background lattice potential: $\hat{\psi}_\sigma(x) = \sum_{j\sigma}\hat{c}_{j\sigma}W(x - x_j)$, where $\hat{c}_{j\sigma}(\hat{c}^\dagger_{j\sigma})$ is the operator annihilating (creating) an atom in the lowest band at site j. Keeping only on-site interactions and neglecting the higher-order corrections to the tunneling by the self-consistent cavity lattice [7,27], we obtain the single-band tight-binding Hamiltonian

$$\begin{aligned}\hat{H} = {} & \left(\Delta_c - M_1\sum_{j,\sigma}\hat{n}_{j\sigma}\right)\hat{a}^\dagger\hat{a} - t\sum_{j,\sigma}(\hat{c}^\dagger_{j\sigma}\hat{c}_{j+1,\sigma} + \text{H.c.}) \\ & + \eta\left(\hat{a}^\dagger + \hat{a}\right)M_0\sum_j(-1)^j(\hat{c}^\dagger_{j\uparrow}\hat{c}_{j\downarrow} + \hat{c}^\dagger_{j\downarrow}\hat{c}_{j\uparrow}) \\ & + \frac{U_s}{2}\sum_j\hat{n}_{j\uparrow}\hat{n}_{j\downarrow} + m_z\sum_j(\hat{n}_{j\uparrow} - \hat{n}_{j\downarrow}), \end{aligned} \tag{A7}$$

where $\hat{n}_{j\sigma} = \hat{c}^\dagger_{j\sigma}\hat{c}_{j,\sigma}$, $t = \int dx\,W^*(x - x_j)[\hat{p}_x^2/2m + V_0\cos^2(k_0x)]W(x - x_{j+1})$, $M_1 = \int dx\,W^*(x - x_j)\cos^2(k_0x)W(x - x_j)$, $M_0 = \int dx\,W^*(x - x_0)\cos(k_0x)W(x - x_0)$, and $U_s = U\int dx|W(x - x_j)|^4$. The factor $(-1)^j$ in above equation results from the spatial dependence of the Raman potential [the last term in Eq. (A5)], which has twice the period of the background lattice potential. The Raman potential and the on-site spin-flipping terms hence have opposite signs on adjacent sites. In the limit of the vanishing Zeeman field m_z, Eq. (A7) reduces to Hamiltonian (1) in the main text.

APPENDIX B: MAGNETIC ORDERS UNDER A FINITE ZEEMAN FIELD

We show the impact of a finite Zeeman field m_z on the spin structure factors and spin correlation functions. As shown in Fig. 5 (top row), when the Zeeman field is small, signals of all phases in Fig. 3 are still present. The phase diagram is therefore robust against a small Zeeman field. However, when the Zeeman field becomes larger, as illustrated in Fig. 5 (bottom row), the spins get polarized along the z direction, such that the system remains ferromagnetic even for $U_l < 0$. The magnetic correlations along the x direction are more robust and persist at the larger Zeeman field.

APPENDIX C: DETERMINATION OF THE PHASE BOUNDARY

In the main text, we identify different magnetic orders using the position of the highest peak in the spin structure factor. As we discuss in the main text, the phase boundaries determined in this manner agree well with the sign of the spin correlation function $C_\alpha(r)$ ($\alpha = x$ and z), i.e., $C_\alpha(r)$ oscillates around 0 in phases with antiferromagnetic correlations or incommensurate antiferromagnetic correlations but stays purely positive in phases with ferromagnetic correlations.

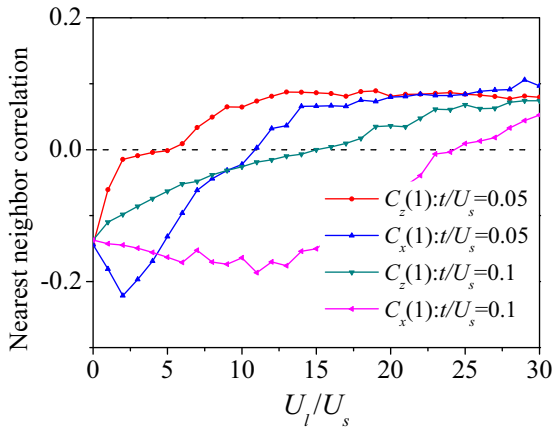

FIG. 6. The nearest-neighbor correlation $C_\alpha(r=1)$ ($\alpha = x$ and z) as a function of the interaction strength U_l calculated for different t/U_s.

The validity of this criterion is further supported by the sign of the nearest-neighbor correlation function $C_\alpha(r=1)$ ($\alpha = x$ and z), as recently discussed in Refs. [49,53]. In Fig. 6, we show the evolution of $C_\alpha(r=1)$ as a function of U_l/U_s for two representative values of t/U_s. Compared to corresponding points in the phase diagram shown in Fig. 3, it is clear that positions of the sign change in $C_\alpha(r=1)$ coincide with the phase boundaries between the ferromagnetic phase boundaries.

APPENDIX D: FINITE-SIZE SCALING

We show the finite-size scaling of four representative points in the phase diagram in Fig. 7. It is apparent that the critical points remain finite in the thermodynamic limit $L \longrightarrow \infty$, which confirms the validity of the phase diagram in the main text.

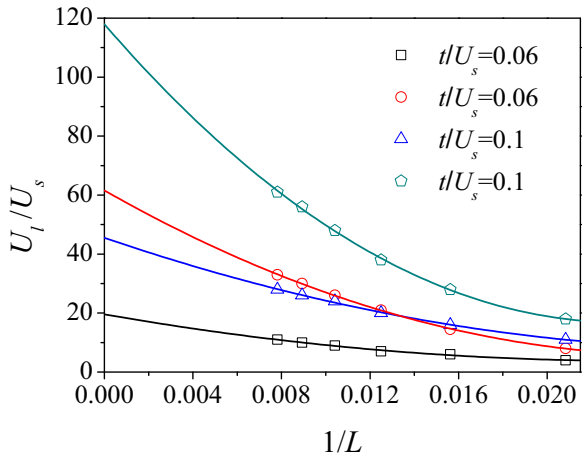

FIG. 7. The finite-size scaling of the critical interaction strength U_l calculated for two different values of t/U_s. The scaling function is a second-order polynomial in $1/L$.

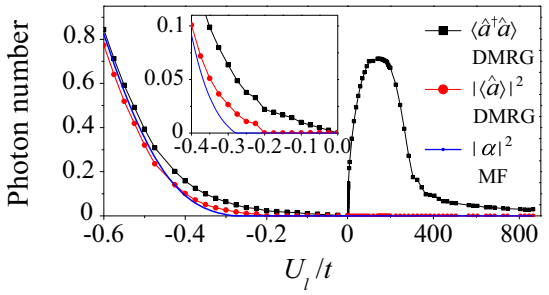

FIG. 8. Comparison of the cavity photon number $|\alpha|^2$ from the mean-field (MF) calculation (blue), as well as the square of the cavity field $|\langle\hat{a}\rangle|^2$ (red) and the photon number $\langle\hat{a}^\dagger\hat{a}\rangle$ (black) from the DMRG calculations. We focus on the case with $\tilde{\delta}/t = 10$, $U_s = 0$, and $L = 64$.

APPENDIX E: SELF-CONSISTENT MEAN-FIELD CALCULATION OF THE CAVITY FIELD

In the absence of the on-site interaction ($U_s = 0$), the superradiance of the cavity field can be characterized under the mean-field approximation.

We start from the tight-binding Hamiltonian (1) in the main text. Employing the local unitary transformation $\hat{c}_{j\uparrow} \rightarrow (-1)^j \hat{c}_{j\uparrow}$, the Hamiltonian becomes

$$\hat{H} = -\tilde{\delta}\hat{a}^\dagger\hat{a} - t\sum_{j,\sigma}(\hat{c}^\dagger_{j\sigma}\hat{c}_{j+1,\sigma} + \text{H.c.}) + \eta\left(\hat{a}^\dagger + \hat{a}\right)M_0\sum_j(\hat{c}^\dagger_{j\uparrow}\hat{c}_{j\downarrow} + \hat{c}^\dagger_{j\downarrow}\hat{c}_{j\uparrow}). \quad \text{(E1)}$$

The Heisenberg equation for $\hat{a}$ is

$$\partial_t\hat{a} = (i\tilde{\delta} - \kappa)\hat{a} - i\eta M_0\sum_j(\hat{c}^\dagger_{j\uparrow}\hat{c}_{j\downarrow} + \hat{c}^\dagger_{j\downarrow}\hat{c}_{j\uparrow}), \quad \text{(E2)}$$

where the parameter $\tilde{\delta}$ is defined in the main text. Under the mean-field approximation $\langle\hat{a}\rangle = \alpha$ and using the steady-state condition $\partial_t\alpha = 0$, we have

$$\alpha = \frac{\eta M_0}{i\kappa + \tilde{\delta}}\sum_j\langle\hat{c}^\dagger_{j\uparrow}\hat{c}_{j\downarrow} + \hat{c}^\dagger_{j\downarrow}\hat{c}_{j\uparrow}\rangle. \quad \text{(E3)}$$

Note that the cavity is assumed to be in a coherent state under the mean-field approximation, with the average photon number given by $|\alpha|^2$.

The cavity field α can be calculated self-consistently as the following: (i) diagonalize the Hamiltonian ((E1)) from an initial value of the cavity-field α_0; (ii) determine the chemical potential from the number equation $N = \sum_{j,\sigma}\langle\hat{c}^\dagger_{j\sigma}\hat{c}_{j\sigma}\rangle$; (iii) update the cavity field α with Eq. (E3); and (iv) replace α_0 with the current value of α and repeat steps (i)–(iii) until α converges. In Fig. 8, we show the calculated average photon number $|\alpha|^2$ (blue). For comparison, we have also plotted $|\langle\hat{a}\rangle|^2$ (red) and the photon number $\langle\hat{a}^\dagger\hat{a}\rangle$ (black) from the DMRG calculations. From the mean-field results, it is apparent that the system is superradiant for $U_l/t < -0.3$. In the superradiant regime, the mean-field average photon number $|\alpha|^2$ agrees well with both $|\langle\hat{a}\rangle|^2$ and $\langle\hat{a}^\dagger\hat{a}\rangle$ from the DMRG calculations. However, for $U_l > 0$, the system is

not superradiant, as both $|\alpha|^2$ and $|\langle\hat{a}\rangle|^2$ vanish while $\langle\hat{a}^\dagger\hat{a}\rangle$ remains finite. The finite photon number $\langle\hat{a}^\dagger\hat{a}\rangle$ is the result of cavity-field fluctuations, whose effects on the fermions are beyond the mean-field description. We note that the overall picture here is consistent with Fig. 4 in the main text, where a finite on-site interaction is considered.

[1] H. Ritsch, P. Demokos, F. Brennecke, and T. Esslinger, Cold atoms in cavity-generated dynamical optical potentials, Rev. Mod. Phys. **85**, 553 (2013).

[2] K. Baumann, C. Guerlin, F. Brennecke, and T. Esslinger, Dicke quantum phase transition with a superfluid gas in an optical cavity, Nature (London) **464**, 1301 (2010).

[3] J. Lénard, A. Morales, P. Zupancic, T. Esslinger, and T. Donner, Supersolid formation in a quantum gas breaking continuous translational symmetry, Nature (London) **543**, 87 (2017).

[4] J. Lénard, A. Morales, P. Zupancic, T. Donner, and T. Esslinger, Monitoring and manipulating Higgs and Goldstone modes in a supersolid quantum gas, Science **358**, 1415 (2017).

[5] R. Mottl, F. Brennecke, K. Baumann, R. Landig, T. Donner, and T. Esslinger, Roton-type mode softening in a quantum gas with cavity-mediated long-range interactions, Science **336**, 1570 (2012).

[6] J. Klinder, H. Keßler, M. R. Bakhtiari, M. Thorwart, and A. Hemmerich, Observation of a Superradiant Mott Insulator in the Dicke-Hubbard Model, Phys. Rev. Lett. **115**, 230403 (2015).

[7] R. Landig, L. Hruby, N. Dogra, M. Landini, R. Mottl, T. Donner, and T. Esslinger, Quantum phases from competing short- and long-range interactions in an optical lattice, Nature (London) **532**, 476 (2016).

[8] L. Hruby, N. Dogra, M. Landini, T. Donner, and T. Esslinger, Metastability and avalanche dynamics in strongly-correlated gases with long-range interactions, PNAS **115**, 3279 (2018).

[9] S. F. Caballero-Benitez and I. B. Mekhov, Quantum Optical Lattices for Emergent Many-Body Phases of Ultracold Atoms, Phys. Rev. Lett. **115**, 243604 (2015).

[10] M. R. Bakhtiari, A. Hemmerich, H. Ritsch, and M. Thorwart, Nonequilibrium Phase Transition of Interacting Bosons in an Intra-Cavity Optical Lattice, Phys. Rev. Lett. **114**, 123601 (2015).

[11] N. Dogra, F. Brennecke, S. D. Huber, and T. Donner, Phase transitions in a Bose-Hubbard model with cavity-mediated global-range interactions, Phys. Rev. A **94**, 023632 (2016).

[12] Y. Chen, Z. Yu, and H. Zhai, Quantum phase transitions of the Bose-Hubbard model inside a cavity, Phys. Rev. A **93**, 041601(R) (2016).

[13] T. Flottat, L. de Forges de Parny, F. Hébert, V. G. Rousseau, and G. G. Batrouni, Phase diagram of bosons in a two-dimensional optical lattice with infinite-range cavity-mediated interactions, Phys. Rev. B **95**, 144501 (2017).

[14] J. Panas, A. Kauch, and K. Byczuk, Spectral properties and phase diagram of correlated lattice bosons in an optical cavity within bosonic dynamical mean-field theory, Phys. Rev. B **95**, 115105 (2017).

[15] W. Zheng and N. R. Cooper, Superradiance Induced Particle Flow via Dynamical Gauge Coupling, Phys. Rev. Lett. **117**, 175302 (2016).

[16] C. Kollath, A. Sheikhan, S. Wolff, and F. Brennecke, Ultracold Fermions in a Cavity-Induced Artificial Magnetic Field, Phys. Rev. Lett. **116**, 060401 (2016).

[17] A. Sheikhan, F. Brennecke, and C. Kollath, Cavity-induced chiral states of fermionic quantum gases, Phys. Rev. A **93**, 043609 (2016).

[18] K. E. Ballantine, B. L. Lev, and J. Keeling, Meissner-Like Effect for a Synthetic Gauge Field in Multimode Cavity QED, Phys. Rev. Lett. **118**, 045302 (2017).

[19] C.-M. Halati, A. Sheikhan, and C. Kollath, Cavity-induced artificial gauge field in a Bose-Hubbard ladder, Phys. Rev. A **96**, 063621 (2017).

[20] Y. Deng, J. Cheng, H. Jing, and S. Yi, Bose-Einstein Condensates with Cavity-Mediated Spin-Orbit Coupling, Phys. Rev. Lett. **112**, 143007 (2014).

[21] B. Padhi and S. Ghosh, Spin-orbit-coupled Bose-Einstein condensates in a cavity: Route to magnetic phases through cavity transmission, Phys. Rev. A **90**, 023627 (2014).

[22] J.-S. Pan, X.-J. Liu, W. Zhang, W. Yi, and G.-C. Guo, Topological Superradiant States in a Degenerate Fermi Gas, Phys. Rev. Lett. **115**, 045303 (2015).

[23] A. Sheikhan, F. Brennecke, and C. Kollath, Cavity-induced generation of nontrivial topological states in a two-dimensional Fermi gas, Phys. Rev. A **94**, 061603 (2016).

[24] F. Mivehvar, H. Ritsch, and F. Piazza, Superradiant Topological Peierls Insulator inside an Optical Cavity, Phys. Rev. Lett. **118**, 073602 (2017).

[25] L. Dong, C. Zhu, and H. Pu, Photon-induced spin-orbit coupling in ultracold atoms inside optical cavity, Atoms **3**, 182 (2015).

[26] C. Zhu, L. Dong, and H. Pu, Effects of spin-orbit coupling on Jaynes-Cummings and Tavis-Cummings models, Phys. Rev. A **94**, 053621 (2016).

[27] C. Maschler, I. B. Mekhov, and H. Ritsch, Ultracold atoms in optical lattices generated by quantized light fields, Eur. Phys. J. D **46**, 545 (2008).

[28] S. Gopalakrishnan, B. L. Lev, and P. M. Goldbart, Emergent crystallinity and frustration with Bose-Einstein condensates in multimode cavities, Nat. Phys. **5**, 845 (2009).

[29] P. Strack and S. Sachdev, Dicke Quantum Spin Glass of Atoms and Photons, Phys. Rev. Lett. **107**, 277202 (2011).

[30] H. Habibian, A. Winter, S. Paganelli, H. Rieger, and G. Morigi, Bose-Glass Phases of Ultracold Atoms Due to Cavity Backaction, Phys. Rev. Lett. **110**, 075304 (2013).

[31] P. Domokos and H. Ritsch, Collective Cooling and Self-Organization of Atoms in a Cavity, Phys. Rev. Lett. **89**, 253003 (2002).

[32] F. Dimer, B. Estienne, A. S. Parkins, and H. J. Carmichael, Proposed realization of the Dicke-model quantum phase transition in an optical cavity QED system, Phys. Rev. A **75**, 013804 (2007).

[33] D. Nagy, G. Konya, G. Szirmai, and P. Domokos, Dicke-Model Phase Transition in the Quantum Motion of a Bose-Einstein Condensate in an Optical Cavity, Phys. Rev. Lett. **104**, 130401 (2010).

[34] J. Keeling, M. J. Bhaseen, and B. D. Simons, Fermionic Superradiance in a Transversely Pumped Optical Cavity, Phys. Rev. Lett. **112**, 143002 (2014).
[35] F. Piazza and P. Strack, Umklapp Superradiance with a Collisionless Quantum Degenerate Fermi Gas, Phys. Rev. Lett. **112**, 143003 (2014).
[36] Y. Chen, Z. Yu, and H. Zhai, Superradiance of Degenerate Fermi Gases in a Cavity, Phys. Rev. Lett. **112**, 143004 (2014).
[37] W. Zheng and N. R. Cooper, Anomalous Diffusion in a Dynamical Optical Lattice, Phys. Rev. A **97**, 021601(R) (2018).
[38] J. Klinder, H. Keßler, M. Wolke, L. Mathey, and A. Hemmerich, Dynamical phase transition in the open Dicke model, Proc. Natl. Acad. Sci. U.S.A. **112**, 3290 (2015).
[39] P. W. Anderson, Antiferromagnetism. Theory of superexchange interaction, Phys. Rev. **79**, 350 (1950).
[40] E. H. Lieb and D. C. Mattis, Theory of ferromagnetism and the ordering of electronic energy levels, Phys. Rev. **125**, 164 (1962).
[41] E. H. Lieb and F. Y. Wu, Absence of Mott Transition in an Exact solution of the Short-Range, One-Band Model in One Dimension, Phys. Rev. Lett. **20**, 1445 (1968).
[42] E. H. Lieb, Two Theorems on the Hubbard Model, Phys. Rev. Lett. **62**, 1201 (1989).
[43] U. Schollwöck, J. Richter, D. J. J. Farnell, and R. F. Bishop, Editors, *Quantum Magnetism* (Springer, Berlin, 2004).
[44] M. Ogata and H. Shiba, Bethe-ansatz wave function, momentum distribution, and spin correlation in the one-dimensional strongly correlated Hubbard model, Phys. Rev. B **41**, 2326 (1990).
[45] R. A. Hart, P. M. Duarte, T.-L. Yang, X. Liu, T. Paiva, E. Khatami, R. T. Scalettar, N. Trivedi, D. A. Huse, and R. G. Hulet, Observation of antiferromagnetic correlations in the Hubbard model with ultracold atoms, Nature (London) **519**, 211 (2015).
[46] C.-C. Chang and S. Zhang, Spatially inhomogeneous phase in the two-dimensional repulsive Hubbard model, Phys. Rev. B **78**, 165101 (2008).
[47] N. C. Costa, T. Mendes-Santos, T. Paiva, R. R. dos Santos, and R. T. Scalettar, Ferromagnetism beyond Lieb's theorem, Phys. Rev. B **94**, 155107 (2016).
[48] S. Daul and R. M. Noack, Ferromagnetic transition and phase diagram of the one-dimensional Hubbard model with next-nearest-neighbor hopping, Phys. Rev. B **58**, 2635 (1998).
[49] D. Greif, T. Uehlinger, G. Jotzu, L. Tarruell, and T. Esslinger, Short-range quantum magnetism of ultracold fermions in an optical lattice, Science **340**, 1307 (2013).
[50] M. Boll, T. A. Hilker, G. Salomon, A. Omran, J. Nespolo, L. Pollet, I. Bloch, and C. Gross, Spin- and density-resolved microscopy of antiferromagnetic correlations in Fermi-Hubbard chains, Science **353**, 1257 (2016).
[51] M. F. Parsons, A. Mazurenko, C. S. Chiu, G. Ji, D. Greif, and M. Greiner, Site-resolved measurement of the spin-correlation function in the Fermi-Hubbard model, Science **353**, 1253 (2016).
[52] L. W. Cheuk, M. A. Nichols, K. R. Lawrence, M. Okan, H. Zhang, E. Khatami, N. Trivedi, T. Paiva, M. Rigol, and M. W. Zwierlein, Observation of spatial charge and spin correlations in the 2D Fermi-Hubbard model, Science **353**, 1260 (2016).
[53] F. Görg, M. Messer, K. Sandholzer, G. Jotzu, R. Desbuquois, and T. Esslinger, Enhancement and sign reversal of magnetic correlations in a driven quantum many-body system, Nature (London) **553**, 481 (2018).
[54] X.-F. Zhou, K. Zhang, J.-J. Liang, G. Chen, and S.-T. Jia, Spin-orbit coupled repulsive Fermi atoms in a one-dimensional optical lattice, New. J. Phys. **17**, 093044 (2015).
[55] X. Li, Cross Dimensionality and Emergent Nodal Superconductivity with p-orbital Atomic Fermions, arXiv:1705.09686.
[56] A. Mazurenko, C. S. Chiu, G. Ji, M. F. Parsons, M. Kanász-Nagy, R. Schmidt, F. Grusdt, E. Demler, D. Greif, and M. Greiner, A cold-atom Fermi-Hubbard antiferromagnet, Nature (London) **545**, 462 (2017).
[57] R. Landig, F. Brennecke, R. Mottl, T. Donner, and T. Esslinger, Measuring the dynamic structure factor of a quantum gas undergoing a structural phase transition, Nat. Commun. **6**, 7046 (2015).
[58] M. Landini, N. Dogra, K. Kröger, L. Hruby, T. Donner, and T. Essilinger, Formation of a Spin Texture in a Quantum Gas Coupled to a Cavity, Phys. Rev. Lett. **120**, 223602 (2018).